Nanoscale Advances

ROYAL SOCIETY OF CHEMISTRY

PAPER

View Article Online
View Journal | View Issue

Open Access Article. Published on 26 February 2021. Downloaded on 5/24/2026 6:48:22 AM.
This article is licensed under a Creative Commons Attribution-NonCommercial 3.0 Unported Licence.

Check for updates

Cite this: *Nanoscale Adv.*, 2021, **3**, 2334

Aqueous synthesis of composition-tuned defects in $CuInSe_2$ nanocrystals for enhanced visible-light photocatalytic H_2 evolution†

Senlin Qu,[a] Xin Yuan,[a] Yu Li,[a] Xingyang Li,[a] Xiujuan Zhou,[a] Xiaogang Xue,[ab]* Kexiang Zhang,[a] Juan Xu[a] and Changlai Yuan*[a]

The composition and defect tolerance of $CuInSe_2$ (CISe) quantum dots (QDs) provide a scaffold to design defects *via* tailoring the elemental ratio or distributions for boosting photocatalytic H_2 evolution (PHE). Herein, a ligand-assisted two-step aqueous method was developed to prepare defect CISe quantum dots for the first time. UV-vis, XPS, HRTEM, and HADDF investigations confirmed the typical double-absorption edges of copper vacancy defects and indium substituted at copper site defects in the structure constructed through initial synthesis tuned by Cu/In ratio and the ensued coarsening. The steady-transient PL suggested that the D–A recombination with prolonged PL lifetime dominated the emission of composition-optimized $CuInSe_2$ with the Cu/In ratio of 1/4 (CISe-1/4). Further transient photocurrent and electrochemical impedance spectroscopy investigations demonstrated that surface defects in the structure favor the carriers' separation/transportation. The CISe-1/4 exhibited a superior PHE rate of 722 μmol g^{-1} h^{-1}, about 23 times higher than that of the initially synthesized CISe-1/4 nucleus (31 μmol g^{-1} h^{-1}), with a maximum apparent quantum efficiency (AQE) of 1.3%. The analysis of energy levels and the coulombic interaction energy of electron–hole ($J_{e/h}$) based on Raman, extending UV-vis spectra investigations suggested that surface defects resulted in decreased $J_{e/h}$ of CISe-1/4, favoring the enhanced PHE of this structure. This work is expected to provide a reference for designing effective non-noble metal I–III–VI photocatalysts.

Received 26th January 2021
Accepted 23rd February 2021

DOI: 10.1039/d1na00069a

rsc.li/nanoscale-advances

Introduction

Due to the size-related photoelectric properties, Cd-free composition, unique defect tolerance, multiple photon absorption, and composition-dependent band structure, I–III–VI ($AgInS_2$, $CuInS_2$, $AgInSe_2$, $CuInSe_2$, *etc.*) quantum dots (QDs) have been intensively investigated, not only as non-toxic substitutes to II–VI (CdS, CdSe, PbS, *etc.*) QDs in a wide range of applications, such as biological imaging,[1–3] LED[4,5] and solar energy harvesting,[6–8] but also are explored as ideal platforms for developing new physical effects.[9,10] Among these, I–III–VI QDs, $CuInSe_2$ (CISe) have attracted more recent attention for solar energy conversions, such as solar cells, photocatalytic H_2 evolution (PHE), or CO_2 conversion because of its large exciton Bohr radius (about 10.6 nm) that allows tailoring of energy band gaps (E_g) covering a wide light-absorption range from ultraviolet to the red edge of the solar spectrum.[6,7,11,12] More importantly, the unique defect tolerance and composition-related band structure add flexibility in the tailoring of band alignment, either fit well with the redox potential of targeting substances needed for specific photochemical conversions or coupling with other semiconductors for enhancing charge carriers' transfer/separation.[7,13–18]

The dependence of the band gap on the size or I/III elemental ratio of $CuInS_2$ or $AgInS_2$ QDs was investigated originally to tune PL of these QDs;[19] sizes or composition tailoring has been widely explored for boosting PHE of I–III–VI compounds, mainly based on organic synthesis protocols.[4,20–23] For instance, Kameyama *et al.* investigated the combined influences of size and composition on PHE of Zn alloyed $AgInS_2$, confirming that $AgInS_2$ with superior PHE performance share a similar average diameter of about 4.2–5.5 nm and E_g of 2.3–2.4 eV.[24] Torimoto *et al.* demonstrated a superior PHE for a sphere, rod, or rice-shaped Zn alloyed $AgInS_2$ at size/composition groups having a relatively narrow E_g range (from 2.0 eV to 2.6 eV),[25] suggesting the importance of band alignments. Moreover, deep level defects play critical roles in determining the PHE performance among different morphologies.

[a]School of Materials Science and Engineering, Guangxi Key Laboratory of Information Materials, Guilin University of Electronic Technology, Guilin 541004, People's Republic of China. E-mail: liangzixue@163.com; Fax: +86-773-2290810; Tel: +86-773-2290810

[b]State Key Laboratory of Structural Chemistry, Fujian Institute of Research on the Structure of Matter, Chinese Academy of Sciences, Fuzhou, Fujian 350002, P. R. China

† Electronic supplementary information (ESI) available: EDS apparent concentration of CISe QDs with various Cu/In ratios, PL spectra peak separation fitting of CISe-1/4, the flat band potential (E_{fb}) of CISe QDs with various Cu/In ratios. See DOI: 10.1039/d1na00069a

© 2021 The Author(s). Published by the Royal Society of Chemistry

Open Access Article. Published on 26 February 2021. Downloaded on 5/24/2026 6:48:22 AM.
This article is licensed under a Creative Commons Attribution-NonCommercial 3.0 Unported Licence.

Intro-band states derived from various defects were found to facilitate exciting enhancements in $CuInSe_2$ QD-based solar cells.[7,26] However, the $CuInSe_2$ QDs remain unexploited for their PHE applications. Besides, previous reports have been focused on composition-dependent band levels of ternary semiconductors. Defects closely associated with composition employed during synthesis, as carriers' transportation bridge between QDs and reactants or active sites for reactions, however, have rarely been investigated for their relation with PHE performance. Especially, in an aqueous solution, the different reaction rates or K_{sp} between Cu^+ with Se^{2-} and In^{3+} with Se^{2-} provide a chance to construct $CuInSe_2$ surface defects *via* control of growth kinetics.

In this contribution, an aqueous synthesis method was developed for CISe QDs with the CISe surface defects tuned through Cu/In ratio. CISe synthesized in the aqueous phase has good hydrophilicity without ligand exchange. The PHE performance of CISe tuned through Cu/In ratio was analyzed. In combination with structural characterization and composition analysis, steady-transient PL investigations, cyclic voltammetry, electrochemical impedance spectroscopy (EIS), photocurrent, and LSV were used to analyze the correlation between Cu/In ratio and PHE performance to reveal the roles of various defects and mechanisms for enhancing PHE activity of CISe. This work is expected to provide an in-depth understanding of designing Cd-free and noble-metal-free photocatalysts *via* defect engineering.

Results and discussion

CISe QDs with different Cu/In ratios were obtained by the combination of changing copper supply during synthesis. The surface defects of CISe were achieved by a ligand-assisted low-temperature aqueous synthesis and following high-temperature growth, which kinetically separates the In-rich reaction or the nucleus from the followed growth. As Scheme 1 depicts, In-rich initial state tends to be formed at the initial low-temperature nucleus until reaching precipitation–dissolution equilibrium for In^{3+} because hydrazine can easily chelate Cu^+ to form a stable complex $[Cu(hy)_2]^+$ so as to deter the inclusion of Cu^+ or the formation of binary copper chalcogenides. As temperature and pressure increase in the followed step (*i.e.*, epitaxial growth), more $[Cu(hy)_2]^+$ decomposes and reacts with Se^{2-} to deposit on the In-rich initial state to form a relatively Cu-rich surface (Scheme 1a), energy levels of which can be tuned by the amount of Cu^+. During synthesis *via* organic routes, the less stability of Cu–ligand complex and higher growth temperature generally result in Cu-rich initial state, or uncontrollable composition distribution and bad composition uniformity (Scheme 1b), which was believed to be responsible for the fact that exciton absorption cannot be observed in these organically synthesized I–III–VI QDs. Moreover, Cu^+ and In^{3+} would inversely diffuse from higher to lower concentration domains in QD, forming Cu vacancy (V_{Cu}) or In substituted Cu (In_{Cu}) due to the Kirkendall effect;[27,28] concentration and related carriers' dynamics can be tuned by adjusting the Cu/In ratio during synthesis.

The phase structure of CISe QDs with different Cu/In ratios was detected using XRD. The XRD patterns of a series of samples (Fig. 1a) exhibit diffraction peaks at 27.6°, 45.8°, and 67.0°, fitting well with (111), (220), and (400), respectively, reflections of a cubic phase (PDF#23-0208).[28] The XRD results indicated that CISe-1/2 and CISe-1/4 QDs have relatively higher crystallinity than CISe-1/16 and CISe-1/8, which could be associated with less disordered crystal lattice induced by various internal defects. By using the Scherer equation, the average sizes of CISe with the Cu/In ratios of 1/16, 1/8, 1/4, or 1/2 were calculated to be about 2, 2, 3.5, or 5 nm, respectively (Fig. 1b). Meanwhile, the ratio of Cu/In on the surface of the grown CISe

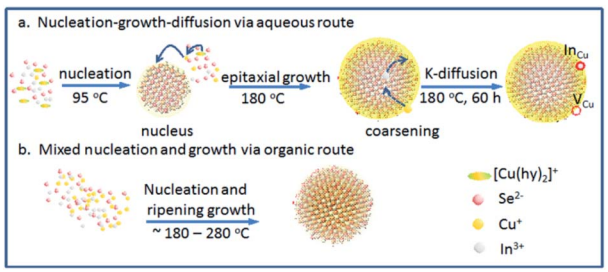

Scheme 1 (a) Ligand-assisted aqueous synthesis and growth *via* nucleus-growth-diffusion route; (b) organic synthesis and growth *via* mixed nucleation and growth.

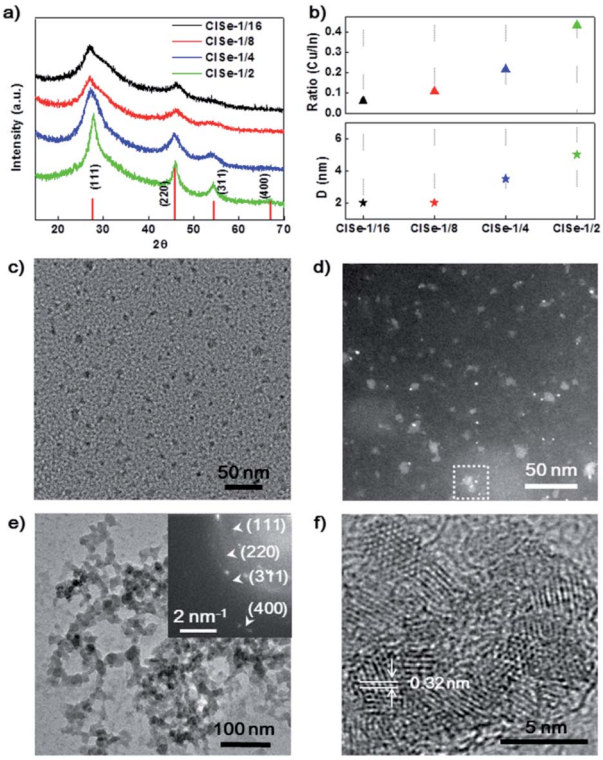

Fig. 1 (a) XRD patterns, (b) EDS measured Cu/In ratio and calculated size of CISe-1/2, CISe-1/4, CISe-1/8, and CISe-1/16; (c) typical TEM of CISe-1/4 initial state CISe nucleus and HAADF at (d) and (e) typical TEM with inset SAED of nucleus grown CISe-1/4 and its HRTEM at (f).

Open Access Article. Published on 26 February 2021. Downloaded on 5/24/2026 6:48:22 AM.
This article is licensed under a Creative Commons Attribution-NonCommercial 3.0 Unported Licence.

measured by EDS (Fig. 1b) is close to that used in each synthesis (see Table S1 and Fig. S2–S5 in ESI†), indicating the complete consumption of metal precursors after 60 hours of growth. Fig. 1c is the TEM image of the CISe-1/4 nucleus, the size of the initial state CISe nucleus is about 1 nm. The HAADF of the CISe-1/4 nucleus is shown in Fig. 1d, the little white bright spots are considered to be In-rich initial state. The initial state CISe-1/4 nucleus is confirmed to be In-rich surface by EDS, Cu/In = 0.195 (see Fig. S1 in ESI†). A typical TEM image (Fig. 1e) of the nucleus grown CISe-1/4 shows that the beaded aggregates are built by CISe QD units. HRTEM observations (Fig. 1f) confirm that the crystalline size is ~3.5 nm, which is consistent with the average crystalline size derived from the XRD. Furthermore, the lattice spacing was measured to be ~0.32 nm, corresponding to the (111) lattice plane of the cubic phase (PDF#23-0208). The inset-selected area electron diffraction (SAED) pattern further confirms the cubic structure of CISe. In comparison, the low-temperature synthesized initial state CISe nucleus or ultra-small QDs exhibit a lower Cu/In ratio than that observed for the high-temperature coarsened nucleus grown CISe (see Table S1 and Fig. S1, S3 in ESI†). It is in agreement with the fact that the selective coordination of hydrazine with Cu^+ facilitates the formation of $[Cu(hy)_2]^+$, which increases the solubility of copper thermodynamically and prohibits the reaction between Cu^+ and Se^{2-} kinetically.[29] Cu^+ can be released *via* the decomposition of $[Cu(hy)_2]^+$ at 180 °C and at a higher pressure and deposited on the In-rich initial state to form a relatively Cu-rich surface forming defects of V_{Cu} or In_{Cu}.

Fig. 2a shows UV-vis absorption spectra of the samples. The inset photograph of samples under daylight indicates that the visible absorption of CISe is enhanced with Cu/In ratio. It is noteworthy that CISe with a Cu/In ratio of 1/16 exhibits a well-defined exciton absorption at 435 nm. Thus far, the well-defined exciton absorption in I–III–VI QDs has rarely been observed, which was ascribed to the inhomogeneous composition of this group materials.[30] Furthermore, another absorption shoulder at 620 nm can be observed to emerge for CISe with Cu/In ratios of 1/4 or 1/2. The double absorption edge is in line with the assumption that the two-step growth results in the formation of compositional defect pairs of CISe, which has two matched band gap generally. Simultaneously, the PL emission of CISe QDs (shown in Fig. 2b) was significantly modified by the Cu/In ratio. CISe with Cu/In ratios of 1/16 or 1/8 displays a relatively narrow emission band centered at 600 nm or 620 nm, while that with 1/4 ratio exhibits a relatively broad emission dominantly centered at 767 nm. Corresponding to the obvious double band edge (Fig. 2a), the PL of CISe-1/4 exhibits the most significantly asymmetric contour, which can be fitted into three peaks centered at 620, 730, and 830 nm (see Fig. S6 in ESI†), which is in agreement with the double-edge of UV-vis spectra of the two samples. The PL of series samples can be divided into two bands centered at ~620 and 767 nm. The high-energy band (600–620 nm) dominated in the PL of CISe-1/16 and CISe-1/8, was previously attributed to a transition of a free electron to a bound hole of the acceptor (F–A),[31,32] formations of which are associated with nucleus states. In comparison, the low-energy band centered at 760 nm observed in CISe-1/4 or CISe-1/2 are assigned to donor–acceptor (D–A) recombination.[31,32] The formation of these defect-related levels can be understood from the two-step preparation of CISe. Various defects, such as indium vacancy (V_{In}), copper vacancy (V_{Cu}), or copper substituting an indium site (Cu_{In}) were reported to possibly act as acceptors.[33] In our Cu-poor synthesis protocols, the copper vacancy (V_{Cu}) defect is more probably to be formed than any other possible acceptors, especially during the low-temperature step. Furthermore, the acceptor ionization energy, which is also in agreement with the previously reported value of V_{Cu},[34] was evaluated to be about 0.43 eV from the emission energy (2.0 eV) and the optical band gap (2.43).[35] By following high temperature coarsening, indium substituted at a copper site (In_{Cu}) and V_{Cu} pairs tend to be formed *via* inverse diffusion of In and Cu driven by the collective distribution of In^{3+} and Cu^+. The main donor levels were evaluated to be ~0.25 eV, which is near the reported value of In_{Cu}.[34,35]

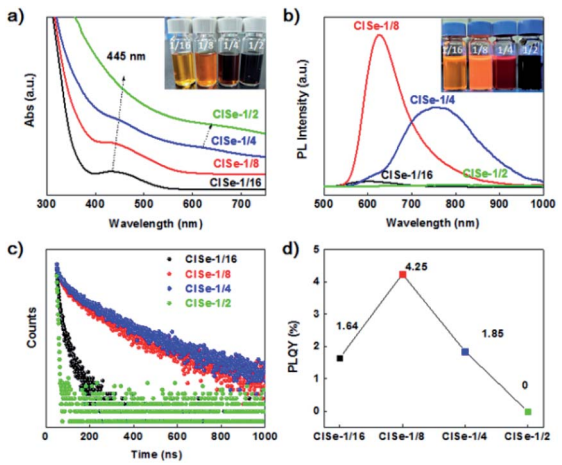

Fig. 2 (a) UV-vis absorption spectra, (b) PL spectra excited at 400 nm, (c) transient PL spectra, and (d) PL QYs of CISe-1/2, CISe-1/4, CISe-1/8, and CISe-1/16. The inset picture is a daylight photograph of QDs, and a dark photograph illuminated by 365 nm ultraviolet light.

The transient PL spectra were measured to detect carriers' recombination rates in samples with different recombination routes. It can be found that the average lifetime of the PL peak increases with an increase in the Cu/In ratio (Fig. 2c). CISe-1/4 has a longer PL lifetime at D–A emission (760 nm, 232 ns) than either the competitive F–A recombination (620 nm, 171 ns) of this sample or PL lifetime of others (see Table S2 in ESI†), suggesting a more rapid or effective carriers' transfer from F–A to D–A. From the aspect of PL intensity, CISe-1/8 has the strongest F–A emission, while CISe-1/4 shows the strongest D–A emission, the efficiency of which can be evaluated from photoluminescence quantum yields (PLQYs) measurements. Fig. 2d exhibits the PLQYs of the sample; it can be observed that QYs increase to a maximum at the Cu/In the ratio of 1/8, and then decreases to a minimum at the Cu/In the ratio of 1/2, where, may be, D–A recombination dominates the emission. This suggests that the quenching could be related to the increments of donors (*i.e.*, In_{Cu}), excessive of which trap photogenerated electrons.[36] This composition distribution enhanced carriers'

 © 2021 The Author(s). Published by the Royal Society of Chemistry

Open Access Article. Published on 26 February 2021. Downloaded on 5/24/2026 6:48:22 AM.
This article is licensed under a Creative Commons Attribution-NonCommercial 3.0 Unported Licence.

transfer would affect PHE or photovoltaic efficiency of samples. For nucleolus CISe, the existence of a high concentration of internal defects formed by low-temperature non-stoichiometric reaction induces internal trapping and bulk recombination. On the contrary, the interfacial defects by increased Cu/In ratio and the following high-temperature coarsening favor the surficial trapping of carriers, which prohibits internal recombination and thus prolong the lifetime of interfacial-defect-related emission. Potentially, this process would boost the internal carriers' separation and transportation toward the interface of QDs, which is also the reaction site for PHE reactions.

The XPS results (Fig. 3) can help to understand the formation of various defects of CISe QDs. The survey spectra (Fig. 3a) confirm the presence of Cu, In, Se, S, and C in samples. The C 1s and S 2p (164 eV) observed on each survey XPS spectrum are mainly ascribed to the modification of the capping ligands. The core-level spectrum of Cu 2p (Fig. 3b) is split into Cu $2p_{3/2}$ (932.3 eV) and Cu $2p_{1/2}$ (952.1 eV), confirming that the chemical state of copper is Cu^{+}.[37] With the increase in the ratio of Cu/In, the peak area increases obviously, indicating the decrease in V_{Cu}. In Fig. 3c, the peaks at 444.8 eV and 452.3 eV are ascribed to In 3d.[37] Intensities of In 3d decreased with an increase in the Cu/In ratio to be the minimum for CISe-1/4 or CISe-1/2. Meanwhile, the binding energy of In 3d moves toward high energy with the increase in the Cu/In ratio during synthesis, which may be related to the formation of In_{Cu} defects. The peaks observed at 54.5 eV or 59.2 eV (Fig. 3d) are corresponding to Se 3d of Se^{2-} or Se^{4+}, respectively.[38] The binding energy of Se 3d moves toward lower energy and can be ascribed to the formation of V_{Cu} or In_{Cu} defects.

Raman spectroscopy was performed to further investigate the variation of defects. As shown in Fig. 4a, the peak centered at 60 cm^{-1} is originating from surface ligand vibration absorption, while the peak centered at 120 or 240 cm^{-1} is assigned to V_{Cu} or In_{Cu}, according to previous reports.[39] In addition, the contour of the Raman spectrum of 1/16 CISe is in line with that theoretically calculated for CISe with 100% concentration of V_{Cu} or In_{Cu}. It can be observed that Raman absorption of V_{Cu} is relatively decreased with an increase in the Cu/In ratio from 1/16 to 1/4, in comparison with that of In_{Cu}, indicating a decrease in the ratio of V_{Cu} to In_{Cu}. Fig. 4b shows the extending UV-vis-NIR diffuse reflectance spectra exhibiting an absorption shoulder at 1050 nm (V_{Cu}-related absorption) and absorption peaks centered at 1200 nm (In_{Cu}-related absorption) absorption, showing consistent evolution tendency with the results of the Raman spectroscopy. It further confirmed the evolution of V_{Cu} and In_{Cu} with increasing Cu/In ratio, confirming our presumptions about composition-tuned defect variation as depicted in Scheme 1.

The photocatalytic activities of these samples were further investigated for designing efficient Cd-free QD photocatalysts. Fig. 5a and b show PHE curves and PHE rates of samples. CISe-1/4 exhibits the highest PHE rate of 722 μmol g^{-1} h^{-1}, about 4 times of CISe-1/16 (185 μmol g^{-1} h^{-1}) or 1.7 times of CISe-1/2 (423 μmol g^{-1} h^{-1}). The PHE of CISe-1/4 is 23 times higher than that of the initially synthesized CISe-1/4 nucleus (31 μmol g^{-1} h^{-1}; see Fig. S9 in ESI†). As the first reported PHE application of CISe QDs so far, the PHE rate outperformed that previously reported for many I–III–VI QDs based photocatalysts under the same none-metal-loading conditions.[20,40] The UV-vis spectra and the steady-transient PL investigation confirmed that CISe-1/4 has a double-edged absorption, and D–A recombination dominated emission with a prolonged lifetime, suggesting that corresponding defects in CISe-1/4 kinetically facilitate the coupling of carriers' transportation with surface reactions. As observed in Fig. 5c, for CISe-1/4, after four consecutive cycles, the hydrogen production rate did not drop significantly and maintained it above 80% of the first cycle. The wavelength-dependent AQE of H_2 evolution of CISe-1/4 (Fig. 5d) exhibited a consistent tendency in the absorption spectrum,

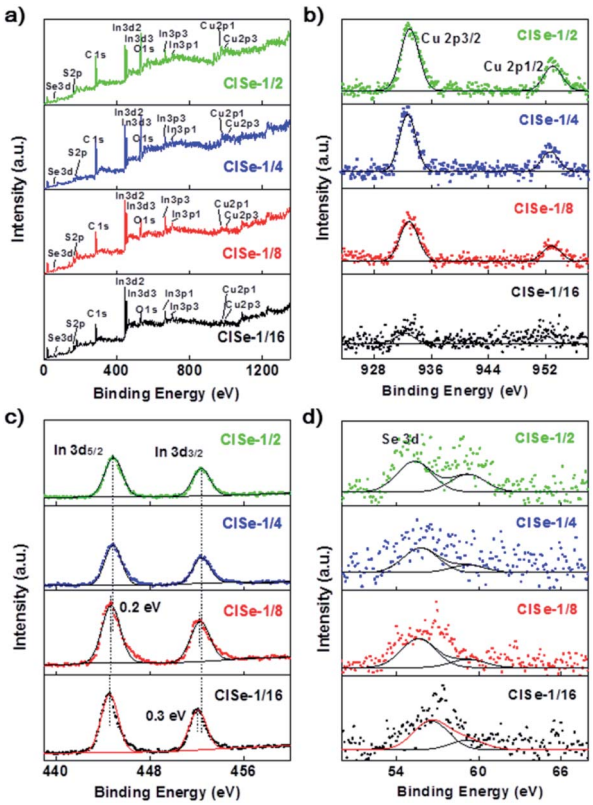

Fig. 3 XPS spectra of CISe-1/2, CISe-1/4, CISe-1/8 and CISe-1/16: (a) survey spectra, (b) Cu 2p, (c) In 3d and (d) Se 3d.

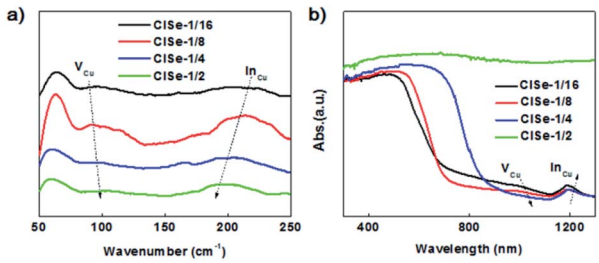

Fig. 4 (a) Raman spectra of CISe QDs with various Cu/In ratios, (b) UV-vis-NIR diffuse reflectance spectra of CISe QDs with various Cu/In ratios.

Open Access Article. Published on 26 February 2021. Downloaded on 5/24/2026 6:48:22 AM.
This article is licensed under a Creative Commons Attribution-NonCommercial 3.0 Unported Licence.

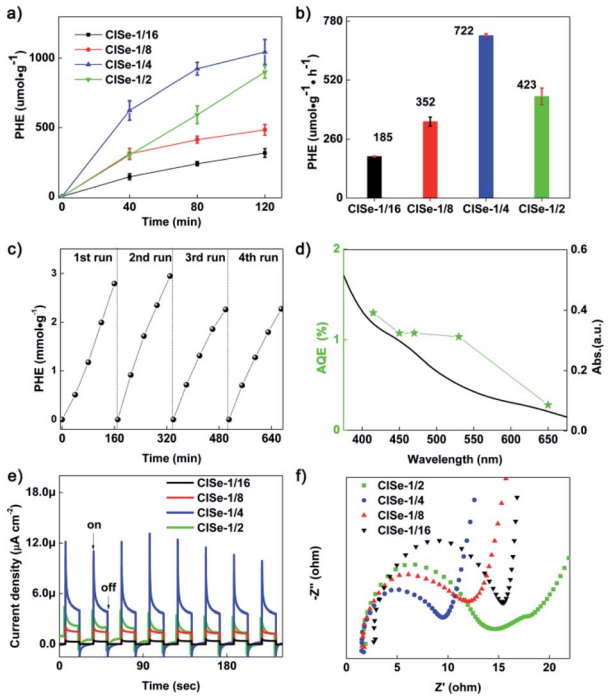

Fig. 5 (a) PHE curves, (b) PHE rates, (c) cycling stability test for H_2 production of CISe-1/4, (d) AQE and UV-Vis absorption spectra of CISe-1/4 QDs, (e) transient photocurrents, (f) EIS Nyquist plots of CISe-1/2, CISe-1/4, CISe-1/8, and CISe-1/16.

with values of 1.1–1.3% at 415 nm, 450 nm, 470 nm, and 550 nm (nearing the band-edge of material).

Fig. 5e shows the transient photocurrent of samples, CISe-1/4 displayed a relatively higher photocurrent in comparison with the other three samples, confirming the enhanced carriers' separation and transportation associated with the composition-tuned double-edge absorption or prolonged PL lifetime. Furthermore, CISe-1/4 or CISe-1/2 showed relatively obvious light-on current decay, in agreement with the D–A recombination dominated PL displayed by the CISe-1/4 or CISe-1/2, suggesting carriers' transfer toward the surface and capture by D–A pairs sited in the surface. In addition, it can be seen that the absolute photocurrent density of the CISe photoanode is consistent with its photocatalytic performance. Moreover, the photocurrent response of CISe-1/4 was enhanced to a maximum immediately after turning on the irradiation light but decreased rapidly to a stable value. The rapid decay of the photocurrent of CISe-1/4 can be ascribed to the sufficient trapping of interfacial defects, which would accumulate electrons or holes to form charge states and need to be consumed by surficial reactions. Kinetically, the accumulation of electrons by active sites promotes the PHE reaction involving the two-electron process.

To further investigate the carriers' separation/transportation in CISe synthesized with different Cu/In ratios, EIS measurements were conducted.[41] EIS Nyquist plots of CISe are shown in Fig. 5f, the radius of the arc on the EIS Nyquist plot reflects the reaction rate occurring at the electrode surface. The smaller arc radius of CISe-1/4 with respect to that of CISe-1/16, CISe-1/8, and CISe-1/2 suggests a more effective separation of photogenerated electrons and holes in CISe In_{Cu} defects and faster interfacial transfer. The EIS Nyquist plot results confirm the superior separation efficiency of electron–hole pairs and transfer of carriers in CISe-1/4.

To assess the photoelectron chemical H_2 generation activity of CISe, linear sweep voltammetry (LSV) was performed. Fig. S12a in ESI† shows LSV curves of samples under chopping visible light. It is worth noting that the photoelectrocatalytic (PEC) activity of CISe samples shares the same order as that of the PHE activity (*i.e.*, CISe-1/4 > CISe-1/2 > CISe-1/8 > CISe-1/16), where CISe-1/4 exhibited the highest PEC activity increased with a negative bias voltage. The photocurrent response of this CISe-1/4 photoanode is constant at about 5 μA cm^{-2} during 1 hour repeated on-off cycling measurements (Fig. S12b in ESI†), indicating a stability of the PEC activity.

The enhanced carriers' separation/transfer was believed to be associated with the band alignments of the composition-tuned In_{Cu} defects of CISe. The optical band gaps (*E*gapopt) of samples can be evaluated from the Tauc plots derived from UV-vis absorption spectra by using the equation:

$$(h\nu\alpha)^{1/n} = A(h\nu - E_{gap}^{opt} \quad (1)$$

where h is the Planck constant, ν is the frequency of electromagnetic waves, and A is a constant. The exponent $n = 2$ is for indirectly allowed transitions and $n = 1/2$ for the direct ones.

Fig. 6a shows the Tauc function for directly allowed transitions and the approximation of the dependence by linear functions for CISe-1/2, −1/4, −1/8, −1/16. Besides the common higher energy linear part (E_{gap}^{opt}, 2.18–2.43 eV) shared by all samples (see Table S3 in ESI†), CISe-1/4 or CISe-1/2 exhibited obvious lower energy part corresponding to 1.80 or 1.73 eV, respectively, which is in agreement with the double-edged absorption for them. The analysis of the Tauc function in the region of low photon energies using the reported procedure[42] revealed that CISe-1/4 and CISe-1/2 contain a CISe with a wide bandgap and an essentially narrower optical gap width, which results in the increased absorption of visible light, in particular at the wavelength between 510 nm to 680 nm. The absorption spectrum-derived bandgap with higher energy is close (2.18–2.43 eV), which can be ascribed to the similar Cu-poor condition generated by the initial formation of $[Cu(hy)_2]^+$. The results confirmed the inhomogeneous deposition between In and Cu during the nucleus/initial growth and the following higher-temperature growth.

The position of LUMO or HOMO can be approximately defined as the reduction or oxidation potential of CISe. The LUMO energy level (*i.e.*, the conduction band level), HOMO energy level (*i.e.*, the valence band level), and the bandgap of CISe were measured using cyclic voltammetry (CV), taking the acetonitrile solution as the electrolyte. The recorded Fig. 6b shows the CV curves of samples. The oxidation and reduction peaks of CISe were determined to be ranging from −1.03 to −1.13 V and 0.99–1.13 V (Table 1), respectively. The positions are generally slightly shifted with the variation of the Cu/In ratio, values of which can be found in Table 1. The energy

 © 2021 The Author(s). Published by the Royal Society of Chemistry

Open Access Article. Published on 26 February 2021. Downloaded on 5/24/2026 6:48:22 AM.
This article is licensed under a Creative Commons Attribution-NonCommercial 3.0 Unported Licence.

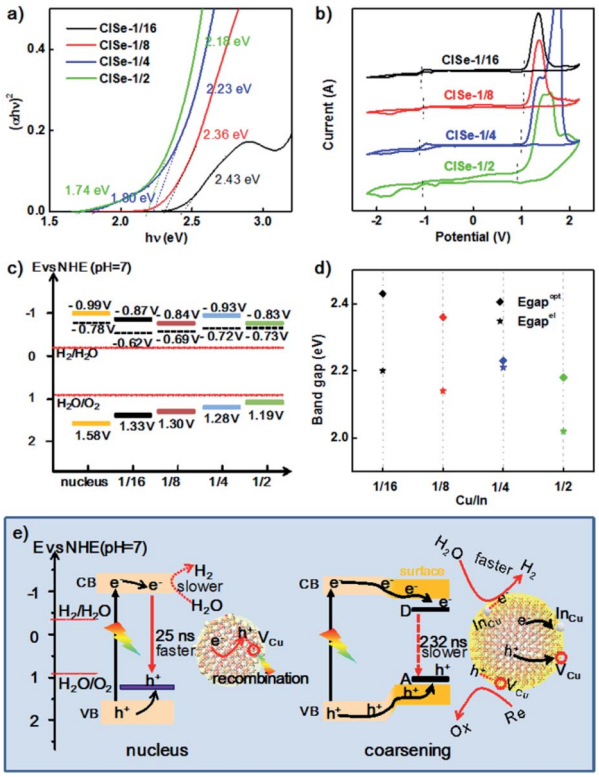

Fig. 6 (a) Tauc plots for evaluating band gaps, (b) cyclic voltammetry curves of E^{OX} and E^{RED}, (c) LUMO, HOMO (solid line) and E_{fb} (black dot line) level alignments, (d) compared E_{gap}^{opt} and E_{gap}^{el} *vs.* Cu/In ratio of CISe-1/2, CISe-1/4, CISe-1/8, and CISe-1/16; (e) scheme illustrating the PHE mechanisms.

Table 1 E^{OX}, E^{RED}, and E_{fb} of CISe QDs sample

Sample	1/4-Nucleus	1/16	1/8	1/4	1/2
E^{OX}	1.38	1.13	1.10	1.08	0.99
E^{RED}	−1.19	−1.07	−1.04	−1.13	−1.03
E_{NHE}^{OX}	1.58	1.33	1.3	1.28	1.19
E_{NHE}^{RED}	−0.99	−0.87	−0.84	−0.93	−0.83
E_{fb}	−0.98	−0.82	−0.89	−0.92	−0.93
$E_{fb\ NHE}$	−0.78	−0.62	−0.69	−0.72	−0.73

levels (HOMO and LUMO) can be obtained from the onset oxidation potential (E^{OX}) and onset reduction potential (E^{RED}), respectively, according to the following equations:

$$E_{HOMO} = -I_P = -(E^{OX} + 4.71) \quad (2)$$

$$E_{LUMO} = -E_a = -(E^{RED} + 4.71) \quad (3)$$

where the measured potential (V) is *vs.* Ag/Ag^+ (0.01 M) reference electrode. It can be observed that the measured electrical bandgap (E_{gap}^{el}) from CV measurements are in agreement with those derived from absorption spectra (Fig. 6c). In fact, thermodynamics can predict the occurrence of hydrogen evolution, and the CISe conduction band is above H_2O/H_2, resulting in spontaneous hydrogen evolution. The flat-band potential (E_{fb}, corresponding to the Fermi level of semiconductor), carrier density, or conduction type of catalyst were determined by the Mott–Schottky curves for understanding the band alignments of samples. The Mott–Schottky curves of all samples (see Fig. S8 in ESI†) exhibited a positively-tangent sloped straight-line part, corresponding to an n-type conductivity. The E_{fb} values of CISe-1/2, −1/4, −1/8, −1/16 are about −0.73, −0.72, −0.69, −0.62 V *vs.* NHE, respectively, (in Table 1), using a conversion previously reported ($E_{Ag/AgCl}$ is the measured value in eqn (4)).

$$E_{NHE} = E_{Ag/AgCl} + 0.197 \quad (4)$$

As such, the band alignments involving the conduction band, valence band, and the Fermi level of the CISe-1/4 nucleus, CISe-1/2, CISe-1/4, CISe-1/8, CISe-1/16 are depicted in Fig. 6c. With increasing Cu/In ratio during synthesis, the position of HOMO or LUMO inversely moves toward positive or negative potentials, resulting in decreased band gaps. Thermodynamically, the conduction bands of samples in the series fit well with the hydrogen evolution reaction. The PHE rates would be more kinetically related to the carriers' separation and transportation toward reactants.

Generally, the higher coulombic interaction energy of electron–hole pairs ($J_{e/h}$) suppresses the charge separation, resulting in slow interfacial charge transfer and low catalytic activity. The values of $J_{e/h}$ can be approximately evaluated by the difference between E_{gap}^{el} and E_{gap}^{opt} using eqn (5).[43]

$$J_{e/h} = E_{gap}^{opt} - E_{gap}^{el} \quad (5)$$

Fig. 6d shows $J_{e/h}$ of various Cu/In ratios samples. It can be observed that CISe-1/4 has the smallest $J_{e/h}$ (0.02 eV), compared to its nucleus (0.53 eV) or other three samples (0.23 eV to 0.16 eV, see Table S3 in ESI†). The decrease of $J_{e/h}$ for CISe-1/4 could be ascribed to the interaction between electron–hole and D–A pair (Fig. 6d), which is in agreement with PL investigations. Raman and extending UV-vis-NIR investigations confirmed that the surficial In_{Cu} defects dominate donor states. Frequently, decreased PL intensity accompanied by decreased native emission lifetime can be observed and ascribed to internal defect-related non-radiative recombination. Thereby, the number of carriers diffused to the surface is decreased, decreasing the PHE activity. However, as for the trapping of carriers by interfacial defects, the attraction between carriers and defects for carriers' trapping would boost the separation of pair of electron–hole and their diffusion toward the surface, which is also the reaction interface for PHE reactions. It is reasonable to assume that these surficial donor states can trap electrons and transport electrons to protons or water for H_2 generation, depicted in Fig. 6e, whereas, holes can be trapped by acceptor states (mainly V_{Cu}) and consumed by sacrificial reagents (S^{2-} and SO_3^{2-}). Transient PL demonstrated that surficial D–A pairs further prolong the lifetime of photogenerated electron–hole (from 25 to 232 ns), favoring coupling carriers' dynamics with photocatalytic PHE reactions.

Open Access Article. Published on 26 February 2021. Downloaded on 5/24/2026 6:48:22 AM.
This article is licensed under a Creative Commons Attribution-NonCommercial 3.0 Unported Licence.

Conclusions

In this work, a procedure for the two-step aqueous synthesis of composition-tuned defect pairs of CISe by the control of Cu/In composition during the nucleus or growth was developed. UV-vis spectra revealed that two-step growth under the Cu/In ratio of 1/4 favored composition-tuned defect pairs with typical double-edged absorption. In agreement with the double-edged absorption, and PL of defects pairs of CISe-1/4 showed unique dual emission bands. CISe-1/4 exhibited enhanced PHE rate of ~722 μmol g^{-1} h^{-1}, about 23 times higher than that of the initially synthesized CISe nucleus (31 μmol g^{-1} h^{-1}). Through analysis, the difference in the PHE of CISe with different Cu/In ratios was mainly attributed to defects. Raman, XPS, and UV-vis-NIR diffuse reflectance spectra confirm that In_{Cu} and V_{Cu} pairs formed *via* inverse diffusion of In and Cu are driven by the collective distribution of In^{3+} and Cu^{+}. Further transient photocurrent, EIS, and other photoelectrochemical investigations suggested that the defects of CISe favor the carriers' separation and transportation. This work is expected to provide a reference for designing effective non-noble metal I–III–VI photocatalysts.

Materials and methods

Chemicals

Copper(I) acetate (CuAc, Strem Chemicals, 97%), indium(III) acetate ($In(Ac)_3$, Alfa Aesar, 99.999%), selenium (Aladdin, ≥99.99% metals basis, ≥200 mesh), trithiocyanuric acid (Macklin, 95%), hydrazine hydrate (hy) aqueous solution (Sinopharm Chemical Reagent Co, Ltd, 85%), sodium sulfide nonahydrate ($Na_2S\cdot 9H_2O$, XiLong Scientific, ≥98%), sodium sulfite (Na_2SO_3, XiLong Scientific, ≥97%), tetrabutylammonium hexafluorophosphate ($TBAPF_6$) were used as purchased and without further purification.

Synthesis of precursors of metal–ligand complexes

0.1 ml of 0.05 M CuAc, 0.1 ml of 0.8 M $In(Ac)_3$ solution, and 1.4 ml of 0.2 M trithiocyanuric acid were loaded in a container. Afterward, the pH of this mixture was adjusted to 9.0 by adding 1.0 M NaOH solution under stirring to achieve a transparent solution of metal–ligand complexes.

Synthesis of Se precursor

0.6 M of selenium was added into 2 ml of hydrazine hydrate aqueous solution (80%) and reacted for 1 hour to obtain $(NH_4)_2Se$ an aqueous solution of hydrazine hydrate. Afterward, freshly prepared $(NH_4)_2Se$ solution was diluted to 20 times the initial concentration in a sealed container and heated to 95 °C.

Synthesis of the CISe nucleus

In a reversal to traditional hot-injection of metal ions to Se cation, Se precursor was poured into the sealed metal–ligand complex solution rapidly, to form a transparent dark grey solution of the initial state CISe. After stirring at 95 °C for 10 min to complete the reaction, the initial state CISe dispersion was prepared and stored for further applications.

The growth of the CISe nucleus to regulate surface defects

60 ml CISe initial state dispersion was sealed into a 100 ml autoclave and the temperature of the autoclave was kept constant at 180 °C in an oven. After growing for a certain time, typically 60 hours, the coarsened CISe dispersion was naturally cooled to room temperature and washed with ethanol to eliminate unreacted ions or ligand coat. The grown $CuInSe_2$ had a Cu/In ratio of 1/16 (CISe-1/16).

The above process was repeated at 0.1 M, 0.2 M, and 0.4 M concentrations of the CuAc solution. The nucleus-grown $CuInSe_2$ nanocrystals were synthesized at the initial Cu/In ratios of 1/8, 1/4, 1/2 (CISe-1/8, CISe-1/4, CISe-1/2).

Characterization

UV-vis and photoluminescence spectra (PL spectra) were obtained on a Lambda 365 spectrophotometer and Edinburgh FS5, respectively. Ultraviolet-visible (UV-vis) diffuse reflection spectra (DRS) were collected from the 200 to 1300 nm range using $BaSO_4$ as the standard reflectance material on the UV-vis spectrophotometer (Shimadzu UV-2450, Japan). All the optical properties were measured at the same concentration. The fluorescence lifetime study was performed on an Edinburgh FL 900 single-photon counting system equipped with a Hamamatsu C8898 picosecond light pulse of 401 nm. Data were analyzed using a non-linear least-squares fitting program, with deconvolution of the exciting pulse being 200 ps. X-ray powder diffraction (XRD) patterns of samples were obtained on a D8 ADVANCE X-ray diffractometer with graphite-monochromated Cu Kα radiation. The surface electronic states and interaction among elements of the samples were detected using X-ray photoelectron spectroscopy (XPS, Thermo ESCALAB 250Xi). Transmission electron microscopy (TEM) and high-resolution TEM (HRTEM) were performed on a Talos F200X 200 kV instrument. The samples for TEM and HRTEM were prepared by placing a drop of a dilute sample on a carbon-film-coated grid. Raman spectra were obtained using a HORIBA LabRAM HR Evolution with laser excitation at 532 nm. $CuInSe_2$ nanocrystals were deposited on Si substrates by spin-coating with absolute ethanol.

The EIS Nyquist plots and photocurrent test were performed on an electrochemical workstation (CHI660E, Chenhua Instruments, Shanghai) in a quartz cell with a three-electrode system, including a Pt counter electrode (2 × 2 cm), an Ag/AgCl reference electrode, and a working electrode, taking a 0.5 M Na_2SO_4 aqueous solution (50 ml) as the electrolyte. The working electrode was prepared as follows: 10 mg of the sample was added to 1 ml deionized water and 20 μl Nafion with ultrasonic dispersion for 1 h to form a uniform slurry. Then, a certain amount of the above slurry (200 μl) was coated smoothly on a 1 cm × 1 cm indium-tin-oxide (ITO) glass. After drying for 12 h, the working electrode was obtained. For the photocurrent test, the light source was a 300 W Xe lamp equipped with a light pass filter (λ > 430 nm), the light on/off was controlled by a timing shutter.

 © 2021 The Author(s). Published by the Royal Society of Chemistry

Open Access Article. Published on 26 February 2021. Downloaded on 5/24/2026 6:48:22 AM.
This article is licensed under a Creative Commons Attribution-NonCommercial 3.0 Unported Licence.

Cyclic voltammograms (CV) were recorded on an electrochemical workstation (CHI600, Chenhua, China) using the glassy carbon disc, Pt wire, and Ag/AgCl reference electrode as the working, counter, or reference electrodes, respectively. 0.1 M $TBAPF_6$ dissolved in acetonitrile was employed as the supporting electrolyte. The working electrodes were polished, cleaned, and dried before the deposition of NC samples. One drop of diluted QDs solution was deposited onto the surface of the working electrode to form a QDs film. The scan rate was set at 50 mV s^{-1}. During all the experiments, electrolyte solutions were thoroughly deoxygenated by bubbling nitrogen gas (99.99%).

Photocatalytic H_2 evolution

Photocatalytic reactions were conducted at approximately 10 °C in a gas-closed inner irradiation system. The light source was a Xenon lamp (Ceaulight CEL-PF300-T8E) equipped with a light pass filter ($\lambda > 430$ nm). An online gas chromatograph (GC7920-TFZ) equipped with a thermal conductivity detector (TCD) and a 5 Å molecular sieve column was employed to analyze the amount of H_2. In a typical test, 0.01 g of CISe QD solids were dispersed in 50 ml of $Na_2S \cdot 9H_2O$ (0.35 M) and Na_2SO_3 (0.25 M) aqueous solutions in the reaction chamber equipped with continuous magnetic stirring under visible light irradiation ($\lambda >$ 430 nm) for H_2 generation. After degassing under vacuum for 30 min, the evolved H_2 was sampled and measured at a certain time interval *via* the online gas chromatograph system. No H_2 was detected in the absence of photocatalyst or light irradiation, indicating the role of CISe QDs for the H_2 generation. The cycling stability tests for H_2 production CISe QDs (0.01 g) (1st run), and after centrifugation and redispersion of QDs into a fresh solution $Na_2S \cdot 9H_2O$ (0.35 M) and Na_2SO_3 (0.25 M) buffer (2nd, 3rd, 4th runs) were performed.

The apparent quantum efficiency (AQE) of the as-prepared photocatalyst was determined by photocatalytic water-splitting H_2 evolution under monochromatic light irradiation ($\lambda =$ 415 nm, 450 nm, 470 nm 550 nm and 650 nm) and calculated using the equation:

$$\mathrm{AQE} = \frac{2 \times \text{number of hydrogen molecules}}{\text{number of incident photon}} \times 100\%$$

Author contributions

All authors have approved the final version of the manuscript.

Conflicts of interest

There are no conflicts to declare.

Acknowledgements

This work was supported by the National Natural Science Foundation of China, Grant (51762011, 51472241), Guangxi Natural Science Foundation, Grant (2016GXNSFAA380040, 2017GXNSFAA198353), Fujian Natural Science Foundation, Grant (2015J01068), Guilin University of Electronic Technology Grant (UF15010Y), the Free Discovery Fund of Guangxi Key Laboratory of Information Materials, Grant (201040-Z).

Notes and references

1 J. H. Shen, Y. F. Li, Y. H. Zhu, X. L. Yang, X. Z. Yao, J. Li, G. J. Huang and C. Z. Li, *J. Mater. Chem. B*, 2015, **3**, 2873–2882.
2 A. Shamirian, O. Appelbe, Q. B. Zhang, B. Ganesh, S. J. Kron and P. T. Snee, *J. Mater. Chem. B*, 2015, **3**, 8188–8196.
3 J. C. Kays, A. M. Saeboe, R. Toufanian, D. E. Kurant and A. M. Dennis, *Nano Lett.*, 2020, **20**, 1980–1991.
4 Y. M. You, X. Tong, W. H. Wang, J. C. Sun, P. Yu, H. N. Ji, X. B. Niu and Z. M. M. Wang, *Adv. Sci.*, 2019, **6**, 1801967.
5 Z. Wang, X. Zhang, W. Xin, D. Yao, Y. Liu, L. Zhang, W. Liu, W. Zhang, W. Zheng, B. Yang and H. Zhang, *Chem. Mater.*, 2018, **30**, 8939–8947.
6 D. Colombara, H. Elanzeery, N. Nicoara, D. Sharma, M. Claro, T. Schwarz, A. Koprek, M. H. Wolter, M. Melchiorre, M. Sood, N. Valle, O. Bondarchuk, F. Babbe, C. Spindler, O. Cojocaru-Miredin, D. Raabe, P. J. Dale, S. Sadewasser and S. Siebentritt, *Nat. Commun.*, 2020, **11**, 3634.
7 J. Du, R. Singh, I. Fedin, A. S. Fuhr and V. I. Klimov, *Nat. Energy*, 2020, **5**, 409–417.
8 K. F. Wu, H. B. Li and V. I. Klimov, *Nat. Photonics*, 2018, **12**, 105–417.
9 K. J. McHugh, L. Jing, A. M. Behrens, S. Jayawardena, W. Tang, M. Gao, R. Langer and A. Jaklenec, *Adv. Mater.*, 2018, **30**, 1706356.
10 C. Tan, J. Chen, X.-J. Wu and H. Zhang, *Nat. Rev. Mater.*, 2018, **3**, 17089.
11 D. Colombara, F. Werner, T. Schwarz, I. C. Infante, Y. Fleming, N. Valle, C. Spindler, E. Vacchieri, G. Rey, M. Guennou, M. Bouttemy, A. G. Manjon, I. P. Alonso, M. Melchiorre, B. El Adib, B. Gault, D. Raabe, P. J. Dale and S. Siebentritt, *Nat. Commun.*, 2018, **9**, 286.
12 D. Cahen, J. M. Gilet, C. Schmitz, L. Chernyak, K. Gartsman and A. Jakubowicz, *Science*, 1992, **258**, 271–274.
13 A. Fuhr, H. J. Yun, S. A. Crooker and V. I. Klimov, *ACS Nano*, 2020, **14**, 2212–2223.
14 D. Moodelly, P. Kowalik, P. Bujak, A. Pron and P. Reiss, *J. Mater. Chem. C*, 2019, **7**, 11665.
15 Q. Yang, S. Zhang, C. Tan, H. Ye, X. Ming, S. Ingebrandt and X. Chen, *J. Mater. Chem. C*, 2017, **5**, 9412–9420.
16 C. Zhang, S. Wei, L. Sun, F. Xu, P. Huang and H. Peng, *J. Mater. Sci. Technol.*, 2018, **34**, 1526–1531.
17 Y. Mao, Y. Li, Y. Zou, X. Shen, L. Zhu and G. Liao, *Ceram. Int.*, 2019, **45**, 1724–1729.
18 Z. Chen, Y. Wu, Q. Wang, Z. Wang, L. He, Y. Lei and Z. Wang, *Prog. Nat. Sci.: Mater. Int.*, 2017, **27**, 333–337.
19 T. Torimoto, T. Adachi, K. Okazaki, M. Sakuraoka, T. Shibayama, B. Ohtani, A. Kudo and S. Kuwabata, *J. Am. Chem. Soc.*, 2007, **129**, 12388–12389.
20 D. Kandi, S. Martha and K. M. Parida, *Int. J. Hydrogen Energy*, 2017, **42**, 9467–9481.

Open Access Article. Published on 26 February 2021. Downloaded on 5/24/2026 6:48:22 AM.
This article is licensed under a Creative Commons Attribution-NonCommercial 3.0 Unported Licence.

21 O. Yarema, M. Yarema, D. Bozyigit, W. M. M. Lin and V. Wood, *ACS Nano*, 2015, **9**, 11134–11142.
22 H. D. Jin and C.-H. Chang, *J. Nanopart. Res.*, 2012, **14**, 1180.
23 A. S. Kshirsagar, P. V. More and P. K. Khanna, *RSC Adv.*, 2016, **6**, 86137–86150.
24 T. Kameyama, T. Takahashi, T. Machida, Y. Kamiya, T. Yamamoto, S. Kuwabata and T. Torimoto, *J. Phys. Chem. C*, 2015, **119**, 24740–24749.
25 T. Torimoto, Y. Kamiya, T. Kameyama, H. Nishi, T. Uematsu, S. Kuwabata and T. Shibayama, *ACS Appl. Mater. Interfaces*, 2016, **8**, 27151–27161.
26 X. Y. Liu, G. B. Braun, H. Z. Zhong, D. J. Hall, W. L. Han, M. D. Qin, C. Z. Zhao, M. N. Wang, Z. G. She, C. B. Cao, M. J. Sailor, W. B. Stallcup, E. Ruoslahti and K. N. Sugahara, *Adv. Funct. Mater.*, 2016, **26**, 267–276.
27 D. Albinsson, S. Nilsson, T. J. Antosiewicz, V. P. Zhdanov and C. Langhammer, *J. Phys. Chem. C*, 2019, **123**, 6284–6293.
28 M. D. Regulacio, Y. Wang, Z. W. Seh and M. Y. Han, *ACS Appl. Nano Mater.*, 2018, **1**, 3042–3062.
29 B. Li, Y. Xie, J. X. Huang and Y. T. Qian, *Adv. Mater.*, 1999, **11**, 1456–1459.
30 R. G. Xie, M. Rutherford and X. G. Peng, *J. Am. Chem. Soc.*, 2009, **131**, 5691.
31 J. Krustok, J. Mädasson and K. Hjelt, *Solid State Commun.*, 1995, **94**, 889–892.
32 F. A. Abouelfotouh, H. Moutinho, A. Bakry, T. J. Coutts and L. L. Kazmerski, *Sol. Cells*, 1991, **30**, 151–160.
33 M. Jean, S. Peulon, J. F. Guillemoles and J. Vedel, *Ionics*, 1997, **3**, 149–154.
34 G. Dagan, F. Abou-Elfotouh, D. J. Dunlavy, R. J. Matson and D. Cahen, *Chem. Mater.*, 1990, **2**, 286–293.
35 S. B. Zhang, S. H. Wei, A. Zunger and H. Katayama-Yoshida, *Phys. Rev. B: Condens. Matter Mater. Phys.*, 1998, **57**, 9642.
36 Y. Jiang, Y. Y. Huang, H. Cheng, Q. H. Liu, Z. Xie, T. Yao, Z. Jiang, Y. Y. Huang, Q. Bian, G. Q. Pan, Z. H. Sun and S. Q. Wei, *J. Phys. Chem. C*, 2014, **118**, 714–719.
37 P. E. Sobol, A. J. Nelson, C. R. Schwerdtfeger, W. F. Stickle and J. F. Moulder, *Surf. Sci. Spectra*, 1992, **1**, 393–397.
38 X. Jin, T. P. Vinod and J. Kim, *J. Nanosci. Nanotechnol.*, 2012, **12**, 5892–5896.
39 D. W. Houck, E. I. Assaf, H. Shin, R. M. Greene, D. R. Pernik and B. A. Korgel, *J. Phys. Chem. C*, 2019, **123**, 9544.
40 M. D. Regulacio and M. Y. Han, *Acc. Chem. Res.*, 2016, **49**, 511–519.
41 H. Chi, J. Liu, X. Zhang, X. Xue, D. Zhang, X. Lin, P. Huang, L. Sun, J. Xiong, P. Cai and J. Zhang, *J. Mater. Chem. C*, 2020, **8**, 9366–9372.
42 A. A. Valeeva, E. A. Kozlova, A. S. Vokhmintsev, R. V. Kamalov, I. B. Dorosheva, A. A. Saraev, I. A. Weinstein and A. A. Rempel, *Sci. Rep.*, 2018, **8**, 9607.
43 M. Amelia, C. Lincheneau, S. Silvi and A. Credi, *Chem. Soc. Rev.*, 2012, **41**, 5728–5743.

 © 2021 The Author(s). Published by the Royal Society of Chemistry